Iivanainen, Joonas; Mäkinen, Antti J.; Zetter, Rasmus; Zevenhoven, Koos C.J.; Ilmoniemi, Risto J.; Parkkonen, Lauri

A general method for computing thermal magnetic noise arising from thin conducting objects

Published in:
Journal of Applied Physics

DOI:
10.1063/5.0050371

Published: 28/07/2021

Document Version
Publisher's PDF, also known as Version of record

Please cite the original version:
Iivanainen, J., Mäkinen, A. J., Zetter, R., Zevenhoven, K. C. J., Ilmoniemi, R. J., & Parkkonen, L. (2021). A general method for computing thermal magnetic noise arising from thin conducting objects. *Journal of Applied Physics*, *130*(4), Article 043901. https://doi.org/10.1063/5.0050371

Journal of Applied Physics

A general method for computing thermal magnetic noise arising from thin conducting objects

Cite as: J. Appl. Phys. **130**, 043901 (2021); https://doi.org/10.1063/5.0050371
Submitted: 15 March 2021 . Accepted: 01 June 2021 . Published Online: 22 July 2021

Joonas Iivanainen, Antti J. Mäkinen, Rasmus Zetter, Koos C. J. Zevenhoven, Risto J. Ilmoniemi, and Lauri Parkkonen

Journal of Applied Physics METHOD scitation.org/journal/jap

A general method for computing thermal magnetic noise arising from thin conducting objects

Cite as: J. Appl. Phys. **130**, 043901 (2021); doi: 10.1063/5.0050371
Submitted: 15 March 2021 · Accepted: 1 June 2021 ·
Published Online: 22 July 2021

View Online Export Citation CrossMark

Joonas Iivanainen,[a] Antti J. Mäkinen, Rasmus Zetter, Koos C. J. Zevenhoven, Risto J. Ilmoniemi, and Lauri Parkkonen

AFFILIATIONS

Department of Neuroscience and Biomedical Engineering, Aalto University School of Science, FI-00076 Aalto, Finland

[a]**Author to whom correspondence should be addressed:** jaiivanainen@gmail.com.
Present address: Sandia National Laboratories, PO Box 5800, Albuquerque, NM 87185-1082, USA.

ABSTRACT

Thermal motion of charge carriers in a conducting object causes magnetic field noise that may interfere with sensitive measurements near the object. In this paper, we describe a method to compute the spectral properties of the thermal magnetic noise from arbitrarily shaped thin conducting objects. The method is based on modeling divergence-free currents on a conducting surface using a stream function and calculating the magnetically independent noise-current modes. By doing this, we obtain the power spectral density of the thermal magnetic noise as well as its spatial correlations and frequency dependence. We also describe a numerical implementation of the method and verify it against analytic formulas. We provide the implementation as a part of the free and open-source software package bfieldtools.

I. INTRODUCTION

Thermal agitation of charge carriers in a conductor causes a fluctuating voltage and current referred to as Johnson–Nyquist noise.[1,2] The thermal current fluctuations in the conductor generate a magnetic field that interferes with nearby magnetically sensitive equipment and measurements. Thermal magnetic noise can, e.g., limit the performance of sensitive magnetometers operating in conducting shields[3–5] and impose constraints on fundamental physics experiments.[6,7] Moreover, it can cause decoherence in trapped atoms[8] and in high-resolution transmission electron microscopy.[9] It is therefore important to estimate the magnetic noise contribution from nearby conductors when designing sensitive experiments and devices.

Thermal magnetic noise from conductors can generally be calculated either using direct approaches where the field noise is computed from the estimated noise currents and their statistics[3,4,6,10] or with reciprocal approaches where the noise is obtained by computing the power loss incurred in the material by a known driving magnetic field.[5,11] In simple geometries, analytical expressions for the magnetic noise can be obtained using either of these two approaches.[3–6,10] In more complicated geometries, noise has to be estimated numerically. Numerical methods using the reciprocal approach have been employed to compute the frequency-dependent magnetic noise[9,12,13] while a method based on the direct approach has been suggested for computing the low-frequency noise arising from thin conductors.[14] More recently, a method to model frequency-dependent magnetic noise from flat conductive shields in the inductance-dominated regime has been suggested.[15]

Here, we outline a direct approach to compute the frequency-dependent magnetic noise (in the quasi-static regime) emanating from a conducting object which can be considered a surface with an arbitrary curvature and small but possibly non-constant thickness. We examine the internal coupling phenomena associated with the surface currents in order to determine the independent modes of the Johnson current.[16] We use a stream-function formalism similar to a previous analytical calculation on an infinite conducting plane[10] and to a semi-analytical computation on a layered grid of conducting square patches.[17] The cross-spectral density of the magnetic noise can be computed based on the current fluctuations of the individual modes described by a set of Langevin equations; the fluctuation amplitudes are given by the equipartition theorem.[10,18] Examination of the individual modes gives an intuitive picture of the field noise phenomena.

We present a numerical implementation of this approach, which uses a discretization of the stream function on a triangle mesh representing the conducting surface. The implementation is applicable to any configuration of conducting surfaces, including curved ones. We demonstrate the estimation of magnetic noise in example geometries and—where possible—compare the results with analytical formulas for verification. The implementation is freely available as a part of the open-source Python software package bfieldtools (https://bfieldtools.github.io).[19,20]

II. THEORY

We consider magnetic noise in the frequency range where the macroscopic Johnson noise current is divergence-free. In other words, the macroscopic charge density does not fluctuate, but the current fluctuations are due to the microscopic thermal motion of charge.[10] This allows us to use a stream-function expression for the surface current.

A. Stream function and surface current

We first briefly introduce the stream-function expression of surface currents and describe how it relates to physical quantities such as power dissipation and inductive energy. Specifically, we assume a thin surface S with conductivity $\sigma(\vec{r})$ and thickness $d(\vec{r})$. A divergence-free surface-current density $\vec{K}$ on S can be expressed with a stream function $\Psi(\vec{r}, t)$[19,21,22] as

$$\vec{K}(\vec{r}, t) = \nabla_{\parallel}\Psi(\vec{r}, t) \times \vec{n}(\vec{r}), \tag{1}$$

where $\vec{n}(\vec{r})$ is the unit surface normal and $\nabla_{\parallel}$ is the tangential gradient on the surface. We further express the stream function as a linear combination $\Psi(\vec{r}, t) = \sum_i s_i(t)\psi_i(\vec{r})$, resulting in

$$\vec{K}(\vec{r}, t) = \sum_i s_i(t)\nabla_{\parallel}\psi_i(\vec{r}) \times \vec{n}(\vec{r}) = \sum_i s_i(t)\vec{k}_i(\vec{r}), \tag{2}$$

where $\vec{k}_i(\vec{r}) \equiv \nabla_{\parallel}\psi_i(\vec{r}) \times \vec{n}(\vec{r})$ are unit-strength spatial patterns of surface-current density and $s_i(t)$ are their time-dependent amplitudes. The magnetic field $\vec{B}$ can be computed from these patterns using the Biot–Savart law,

$$\begin{aligned}\vec{B}(\vec{r}, t) &= \frac{\mu_0}{4\pi}\int_S \vec{K}(\vec{r}\,', t) \times \frac{\vec{r} - \vec{r}\,'}{|\vec{r} - \vec{r}\,'|^3}\, dS' \\ &= \sum_i s_i(t)\frac{\mu_0}{4\pi}\int_S \vec{k}_i(\vec{r}\,') \times \frac{\vec{r} - \vec{r}\,'}{|\vec{r} - \vec{r}\,'|^3}\, dS' = \sum_i s_i(t)\vec{b}_i(\vec{r}),\end{aligned} \tag{3}$$

where μ_0 is the vacuum permeability and $\vec{b}_i(\vec{r})$ is the magnetic field from the pattern $\vec{k}_i$ with a unit amplitude.

The instantaneous power dissipation between patterns $\vec{k}_i$ and $\vec{k}_j$ is[19,22]

$$P_{ij}(t) = s_i(t)s_j(t)\int_S \frac{1}{\sigma(\vec{r})\, d(\vec{r})}\vec{k}_i(\vec{r}) \cdot \vec{k}_j(\vec{r})\, dS = s_i(t)s_j(t)R_{ij}, \tag{4}$$

where R_{ij} is the mutual resistance between the patterns. Similarly, the instantaneous inductive energy between the patterns is given by their mutual inductance M_{ij},[19,22]

$$\begin{aligned}E_{ij}(t) &= \frac{1}{2}s_i(t)s_j(t)\frac{\mu_0}{4\pi}\int_S\int_S \frac{\vec{k}_i(\vec{r}) \cdot \vec{k}_j(\vec{r}\,')}{|\vec{r} - \vec{r}\,'|}\, dS\, dS' \\ &= \frac{1}{2}s_i(t)s_j(t)M_{ij}.\end{aligned} \tag{5}$$

The amplitudes of the patterns evolve according to a coupled equation system[22] (see also the Appendix),

$$\mathbf{M}\frac{d}{dt}\mathbf{s}(t) + \mathbf{R}\mathbf{s}(t) - \mathbf{e}(t) = 0, \tag{6}$$

where $\mathbf{s}$ is a vector containing the pattern amplitudes $\mathbf{s}[i](t) = s_i(t)$, $\mathbf{M}$ and $\mathbf{R}$ are the mutual inductance and resistance matrices with elements $\mathbf{M}[i, j] = M_{ij}$ and $\mathbf{R}[i, j] = R_{ij}$ defined above, and $\mathbf{e}(t)$ gives the electromotive force (emf) that is coupled to the patterns. Equation system (6) is analogous to that of coupled RL circuits, where $\mathbf{s}$ contains the circuit currents. However, quantities such as $\mathbf{M}$ and $\mathbf{R}$ depend on the normalization of the circuit basis functions $\vec{k}_i$, whereas energy quantities such as power dissipation and inductive energy are free of this ambiguity.[22]

B. Magnetic Johnson–Nyquist noise

Next, we investigate how to model the magnetic Johnson–Nyquist noise using the stream-function approach. The thermal current fluctuations are driven by the Johnson emf, which is proportional to a zero-mean Gaussian white-noise process.[18] In this case, Eq. (6) represents coupled Langevin equations.

To determine the statistics of the current fluctuations, we apply the equipartition theorem to the system.[10,18] According to this theorem, in a thermal bath with temperature T, each independent degree of freedom of the system has an average energy of $k_BT/2$, where k_B is the Boltzmann constant. The independent degrees of freedom of the system are given by the eigenvectors of $\mathbf{M}$ as they diagonalize the energy matrix obtained by Eq. (5).

We thus look for independent patterns $\vec{\kappa}_i(\vec{r})$ with a diagonal $\mathbf{M}$ as linear combinations of $\vec{k}_j(\vec{r})$. We further require that the patterns $\vec{\kappa}_i(\vec{r})$ diagonalize $\mathbf{R}$ so that also the Langevin equations (6) decouple. As the inductance and resistance matrices are symmetric positive-definite for an ordinary conductor,[22] these independent patterns can be found, for example, by solving a generalized eigenvalue equation,[21,23] i.e., finding an invertible matrix $\mathbf{V}$ such that

$$\mathbf{R}\mathbf{V} = \mathbf{M}\mathbf{V}\mathbf{\Lambda} \Leftrightarrow \begin{cases}\mathbf{V}^{\mathrm{T}}\mathbf{R}\mathbf{V} = \mathrm{diag}(r_i, \ldots, r_N), \\ \mathbf{V}^{\mathrm{T}}\mathbf{M}\mathbf{V} = \mathrm{diag}(l_i, \ldots, l_N),\end{cases} \tag{7}$$

where $\mathbf{\Lambda} = \mathrm{diag}(\lambda_1,\ldots\lambda_N)$ is a diagonal matrix with $\lambda_i = r_i/l_i$. The independent patterns are given by the columns of the invertible but generally non-unitary matrix $\mathbf{V}$ as $\vec{\kappa}_i(\vec{r}) = \sum_j V_{ji}\vec{k}_j(\vec{r})$.

We can transform Eq. (6) to this new basis,

$$\frac{d}{dt}\mathbf{V}^{\mathrm{T}}\mathbf{M}\mathbf{V}\mathbf{V}^{-1}\mathbf{s}(t) + \mathbf{V}^{\mathrm{T}}\mathbf{R}\mathbf{V}\mathbf{V}^{-1}\mathbf{s}(t) - \mathbf{V}^{\mathrm{T}}\mathbf{e}(t) = 0. \tag{8}$$

By defining $\tilde{\mathbf{s}}(t) = \mathbf{V}^{-1}\mathbf{s}(t)$ and $\tilde{\mathbf{e}}(t) = \mathbf{V}^{\mathrm{T}}\mathbf{e}(t)$, we obtain a set of decoupled Langevin equations

$$\frac{d}{dt}\tilde{s}_i(t) + \lambda_i \tilde{s}_i(t) - \tilde{e}_i(t)/l_i = 0. \tag{9}$$

Effectively, we now have a number of independent RL circuits with time constants $\tau_i = l_i/r_i = 1/\lambda_i$ driven by emfs $\tilde{e}_i(t)$.

The Johnson emf has a white (frequency-independent) power spectral density (PSD) $S_{\tilde{e}_i}$ that can be used to solve the PSD of $\tilde{s}_i$ from the decoupled Langevin equation,[18]

$$S_{\tilde{s}_i}(\omega) = \frac{S_{\tilde{e}_i}}{r_i^2}\frac{1}{1 + (\omega/\lambda_i)^2}, \tag{10}$$

where ω is the angular frequency. The average energy (5) of the ith independent degree of freedom is

$$\begin{aligned}\langle E_i(t)\rangle &= \frac{1}{2} l_i \langle \tilde{s}_i(t)^2\rangle = \frac{1}{2} l_i \frac{1}{2\pi}\int_0^\infty S_{\tilde{s}_i}(\omega)\, d\omega \\ &= \frac{1}{2} l_i \frac{S_{\tilde{e}_i}}{4r_i^2}\lambda_i = \frac{S_{\tilde{e}_i}}{8r_i},\end{aligned} \tag{11}$$

where the brackets $\langle\cdot\rangle$ denote the ensemble average. On the other hand, according to the equipartition theorem, the average energy is $\langle E_i\rangle = \frac{1}{2}k_{\mathrm{B}}T$, which can be used together with Eq. (11) to solve the Nyquist formula for the PSD of the Johnson emf,

$$S_{\tilde{e}_i}(\omega) = 4k_{\mathrm{B}}Tr_i, \tag{12}$$

where r_i is associated with the average power dissipation $\langle P_i(t)\rangle = r_i\langle \tilde{s}_i(t)^2\rangle$.

To compute the cross-spectral density (CSD) of the magnetic noise due to the Johnson current, we note that the Fourier transform of the field from the independent patterns is obtained as

$$\begin{aligned} F\{\vec{B}(\vec{r})\}(\omega) &= F\left\{\sum_i s_i(t)\vec{b}_i(\vec{r})\right\} \\ &= F\left\{\sum_i \tilde{s}_i(t)\vec{\beta}_i(\vec{r})\right\} = \sum_i F\{\tilde{s}_i\}(\omega)\vec{\beta}_i(\vec{r}),\end{aligned} \tag{13}$$

where $\vec{\beta}_i(\vec{r})$ denotes the magnetic field from $\vec{\kappa}_i$. The CSD between magnetic field components at $\vec{r}$ and $\vec{r}\,'$ along unit vectors $\vec{n}$ and $\vec{n}\,'$ is given by

$$\begin{aligned} &\left\langle \vec{n}\cdot F\{\vec{B}(\vec{r})\}^* F\{\vec{B}(\vec{r}\,')\}\cdot\vec{n}\,'\right\rangle \\ &= \left\langle \vec{n}\cdot\left(\sum_i F\{\tilde{s}_i\}^*\vec{\beta}_i(\vec{r})\right)\left(\sum_k F\{\tilde{s}_k\}\vec{\beta}_k(\vec{r}\,')\right)\cdot\vec{n}\,'\right\rangle \\ &= \vec{n}\cdot\left(\sum_i\sum_k \vec{\beta}_i(\vec{r})\langle F\{\tilde{s}_i\}^* F\{\tilde{s}_k\}\rangle\vec{\beta}_k(\vec{r}\,')\right)\cdot\vec{n}\,' \\ &= \vec{n}\cdot\overleftrightarrow{\mathrm{CSD}}_{\vec{B}}(\vec{r},\vec{r}\,',\omega)\cdot\vec{n}\,',\end{aligned} \tag{14}$$

where we defined $\overleftrightarrow{\mathrm{CSD}}_{\vec{B}} = \sum_i\sum_k \vec{\beta}_i(\vec{r})\langle F\{\tilde{s}_i\}^* F\{\tilde{s}_k\}\rangle\vec{\beta}_k(\vec{r}\,')$ as the CSD tensor of the magnetic field.

The CSD tensor can be simplified by noting that the amplitudes $\tilde{s}_i$ are independent: their temporal cross-correlation is $\int \tilde{s}_i(t)\tilde{s}_k(t+t')\,dt = 0$ for $i \neq k$. For $i = k$, the auto-correlation with exponential decay is given as the Fourier transform of the PSD of Eq. (10). The CSD of $\tilde{s}_i$ and $\tilde{s}_k$ is thereby $\langle F\{\tilde{s}_i\}^* F\{\tilde{s}_k\}\rangle = S_{\tilde{s}_i}(\omega)\delta_{ik}$ and the CSD tensor of the magnetic noise is

$$\overleftrightarrow{\mathrm{CSD}}_{\vec{B}}(\vec{r},\vec{r}\,',\omega) = \sum_i \vec{\beta}_i(\vec{r})S_{\tilde{s}_i}(\omega)\vec{\beta}_i(\vec{r}\,'). \tag{15}$$

The above analysis was made for a single conducting surface. The analysis applies similarly for a system comprising multiple separate conductors. In this case, the mutual inductance matrix $\mathbf{M}$ is formed by computing the inductances between all the patterns in the conductors. The resistance matrix $\mathbf{R}$ can be formed as a block matrix comprising the resistance matrices of the individual conductors with the mutual conductivities between patterns in the different conductors being zero. Also, skin effects may potentially be modeled by dividing the conductor into a stack of multiple inductively coupled layers, each of which with a thickness smaller than the skin depth.[24]

Next, we briefly describe how to compute the CSD between field measurements by an array of sensors. We approximate the measurement of the ith sensor $y_i(t)$ as a weighted sum of the magnetic field over the spatial extent of the sensor,

$$y_i(t) = \int \vec{w}_i(\vec{r})\cdot\vec{B}(\vec{r},t)\,dV \approx \sum_{l=1}^{N_i}\vec{w}_i(\vec{r}_l)\cdot\vec{B}(\vec{r}_l,t), \tag{16}$$

where $\vec{r}_l$ are the N_i integration points of the sensor i and $\vec{w}_i(\vec{r}_l)$ are their vector weights. The CSD between measurements y_i and y_k is then

$$\begin{aligned}\mathrm{CSD}_{y_i,y_k}(\omega) &= \left\langle F\{y_i\}^* F\{y_k\}\right\rangle \\ &= \sum_{l=1}^{N_i}\sum_{h=1}^{N_k}\vec{w}_i(\vec{r}_l)^*\cdot\overleftrightarrow{\mathrm{CSD}}_{\vec{B}}(\vec{r}_l,\vec{r}_h,\omega)\cdot\vec{w}_k(\vec{r}_h).\end{aligned} \tag{17}$$

III. IMPLEMENTATION

Here, we briefly outline the numerical implementation of the magnetic noise computation. The implementation is a part of the bfieldtools Python software package[20] and uses its stream-function discretization as well as numerical integrals and functions to compute the resistance and inductance matrices. The theoretical and computational aspects of the software are presented in detail elsewhere.[19]

In bfieldtools, the conducting surface is represented by a triangle mesh and the stream-function basis in the expansion $\Psi(\vec{r}) = \sum_i s_i h_i(\vec{r})$ consists of piecewise linear functions ("hat functions") $h_i(\vec{r})$. The hat function attains a value of one at the vertex i, zero at other vertices, and is linearly interpolated on the triangle faces. Each of these basis functions represents an elementary current pattern, which circulates around the corresponding vertex i. The magnetic field is obtained from the stream function s_i with a linear map [see Eq. (3)]. For example, the z-component of the field at N evaluation points is

$$\mathbf{b}_z = \mathbf{C}\mathbf{s}, \tag{18}$$

where $\mathbf{C}$ is the $N \times M$ matrix that maps the M vertex-circulating currents ($\mathbf{s}[i] = s_i$) to field component amplitudes at the evaluation points.

The resistance matrix $\mathbf{R}$ [with surface conductivity $\sigma(\vec{r})d(\vec{r})$ discretized and assumed constant across each triangle] and inductance matrix $\mathbf{M}$ of the elementary current patterns can be computed using the software. In the case of an open mesh, the boundary conditions of the stream function are set as described in our earlier publication.[19] Multiple separate conductors can be handled by computing the mutual inductances between all the elementary patterns and by forming a block diagonal resistance matrix comprising the resistance matrices of the individual conductors.

We decouple the elementary circuits by solving the generalized eigenvalue Eq. (7) for eigenvalues $\mathbf{\Lambda}$ and eigenvectors $\mathbf{V}$ using SciPy.[25] We then evaluate the CSD matrix $\mathbf{\Sigma_b}$ of the magnetic field component at ω using Eq. (18) as

$$\mathbf{\Sigma_b} = \langle \mathbf{b}_z \mathbf{b}_z^{\mathrm{T}} \rangle = \mathbf{C}\mathbf{V}\langle \tilde{\mathbf{s}}\tilde{\mathbf{s}}^{\mathrm{T}} \rangle \mathbf{V}^{\mathrm{T}}\mathbf{C}^{\mathrm{T}} = \mathbf{C}\mathbf{V}\mathbf{\Sigma}_{\tilde{\mathbf{s}}}\mathbf{V}^{\mathrm{T}}\mathbf{C}^{\mathrm{T}}, \tag{19}$$

where $\mathbf{s} = \mathbf{V}\tilde{\mathbf{s}}$ and $\mathbf{\Sigma}_{\tilde{\mathbf{s}}}$ is a diagonal matrix with elements $\mathbf{\Sigma}_{\tilde{\mathbf{s}}}[i, i] = S_{\tilde{s}_i}(\omega)$ [see Eq. (10)].

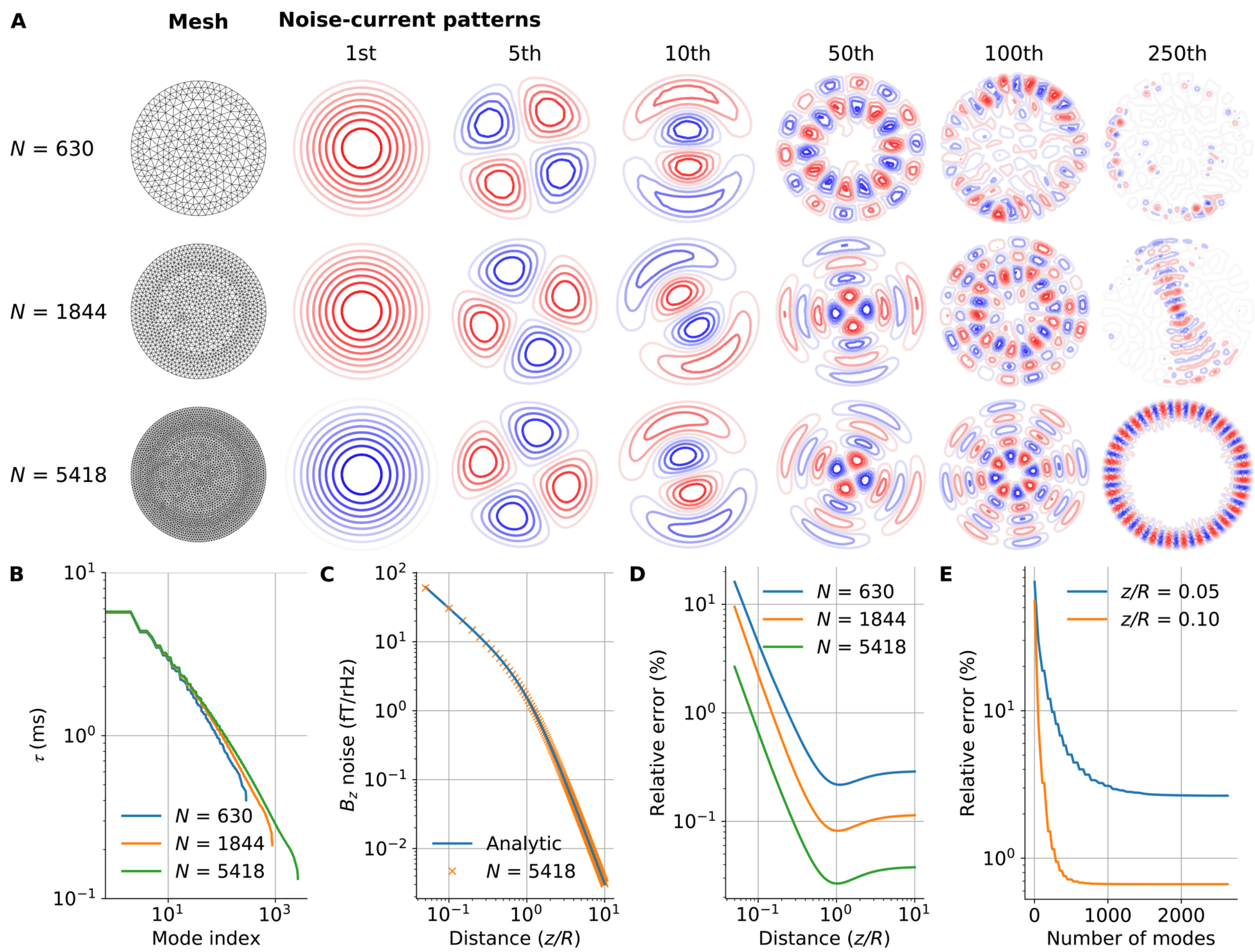

FIG. 1. Comparison of the numerical solution of magnetic thermal noise emanating from a conducting disk with radius $R = 1.0$ m (centered on the xy plane) to an analytical formula. (a) Three meshes with different numbers of triangles (N) representing the disk, and exemplary contours of the numerically solved noise-current patterns. Blue and red contours depict current flow in opposite directions. (b) The time constants τ of the modes computed with the different meshes. [(c) and (d)] Comparison between the numerical and analytical solutions of the low-frequency magnetic noise (B_z) on the z axis. (c) Comparison between the numerical solution obtained using the densest mesh and the analytical formula. (d) The relative errors of the numerical solutions to the analytical formula. (e) Relative error as a function of the number of current modes for the densest mesh.

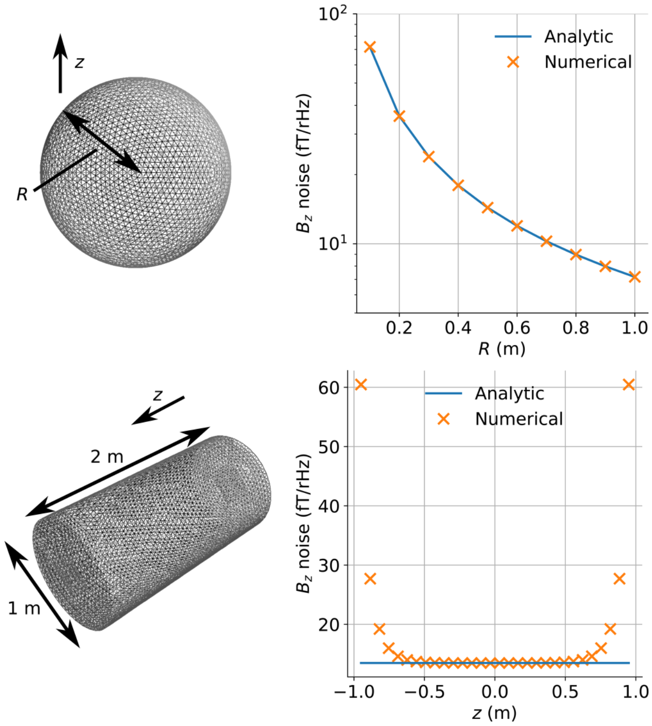

FIG. 2. Numerical computation of low-frequency magnetic noise inside spherical and cylindrical conducting surfaces (represented as triangle meshes) and comparison to results from analytical formulas. Top: Magnetic noise at the center of a sphere with different sphere radii R. Bottom: Noise in the field component along the long axis (z) of the cylinder. The analytical formula only applies at the center of the cylinder ($z = 0$ m).

We model the measurement y_i in Eq. (16) as $y_i = \mathbf{w}_i^{\mathrm{T}}\mathbf{b}_i$, where $\mathbf{w}_i^{\mathrm{T}}$ is a row vector comprising the sensor weights and $\mathbf{b}_i = \mathbf{C}_i\mathbf{s}$ is a column vector of the magnetic noise along the directions of the vector weights at the integration points. The elements of the measurement CSD matrix can then be computed as follows:

$$\Sigma_{\mathbf{y}}[i, k] = \mathbf{w}_i^{\mathrm{T}}\langle \mathbf{b}_i \mathbf{b}_k^{\mathrm{T}} \rangle \mathbf{w}_k = \mathbf{w}_i^{\mathrm{T}}\mathbf{C}_i \mathbf{V} \Sigma_{\tilde{\mathbf{s}}} \mathbf{V}^{\mathrm{T}} \mathbf{C}_k^{\mathrm{T}} \mathbf{w}_k. \tag{20}$$

In practice, we compute the cross-spectral densities using multidimensional NumPy-arrays[26] and by summing over the relevant dimensions of the arrays. This way, we can, e.g., compute the cross-spectral density of the magnetic field in 300 observation points at 100 frequencies and store the result in an array with dimensions of $300 \times 300 \times 3 \times 3 \times 100$.

IV. VALIDATION AND EXAMPLES

We first analyzed special cases that allowed comparing our numerical computation of the magnetic noise with the results from analytical formulas at the low-frequency limit. Specifically, we investigated the following:

- B_z noise along the z axis due to a uniform conducting disk centered on the xy plane;
- B noise at the center of a spherical conducting surface as a function of the sphere radius; and
- B noise at the center of a cylindrical conducting surface along the long axis of the cylinder.

The analytical formulas for these three cases are available in the literature.[5] Besides the validation cases, we present also example computations. Unless stated otherwise, we used $d = 1$ mm and $\sigma = 3.8 \times 10^7\ \Omega^{-1}\mathrm{m}^{-1}$, corresponding to aluminum at room temperature $T = 293$ K.

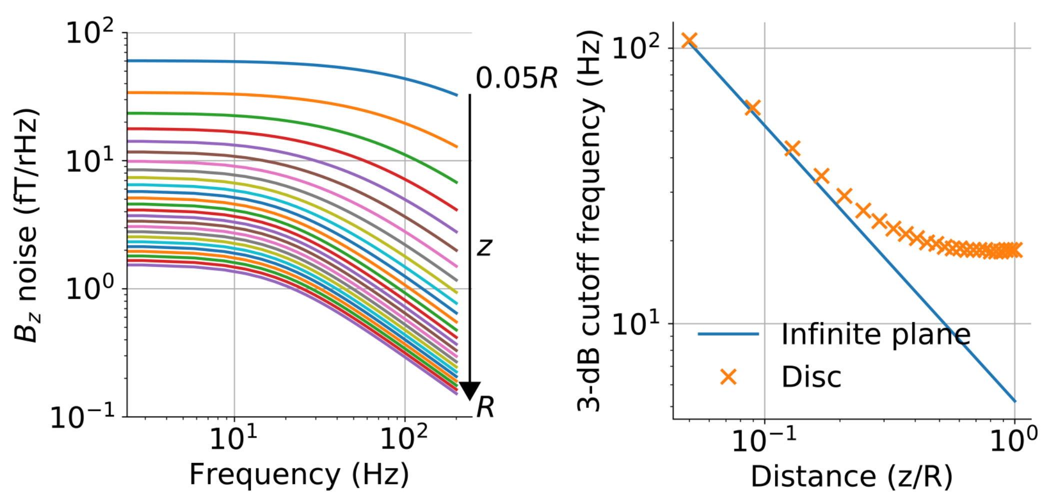

FIG. 3. Spectral density of the thermal magnetic noise B_z on the z axis due to a circular conducting disk with radius $R = 1.0$ m centered on the xy plane. Left: Spectral density as a function of frequency and distance. The curves with different colors represent the noise with different relative distances from the mesh as indicated in the figure. Right: The frequency at which the noise power has decreased by 3 dB from its zero-frequency value. The solid line gives the −3-dB frequencies for an infinite plane, calculated using an analytical formula.

A. Validation cases

Figure 1 presents the computation of the low-frequency B_z noise along the z axis due to a disk with a radius $R = 1.0$ m centered on xy plane. The disk was modeled with three different meshes with 630, 1844, and 5418 triangles. Figure 1(a) shows examples of the stream-function contours of the numerically computed patterns of the noise current while Fig. 1(b) shows their time constants. To model the higher order modes more accurately, denser mesh is needed. At a distance of $z = 0.05R$, the relative error of the numerical solution of B_z noise to the analytical formula is 2.7% when the densest mesh is used; with a larger distance, the relative error is smaller. Compared to the densest mesh, the sparse meshes produce higher relative error regardless of the distance.

Figure 2 shows the numerical results for the low-frequency magnetic noise at the center of a closed sphere (2562 vertices; 5120 triangles) and along the axis of a closed cylinder (3842 vertices; 7680 triangles). The computation and analytical formulas agree with relative errors of 0.06% and 0.03%, respectively.

B. Examples

We examined the magnetic noise and its frequency dependence using a simple conductor. We computed the B_z noise on the z axis as well as the magnetic noise CSD along the x axis due to a

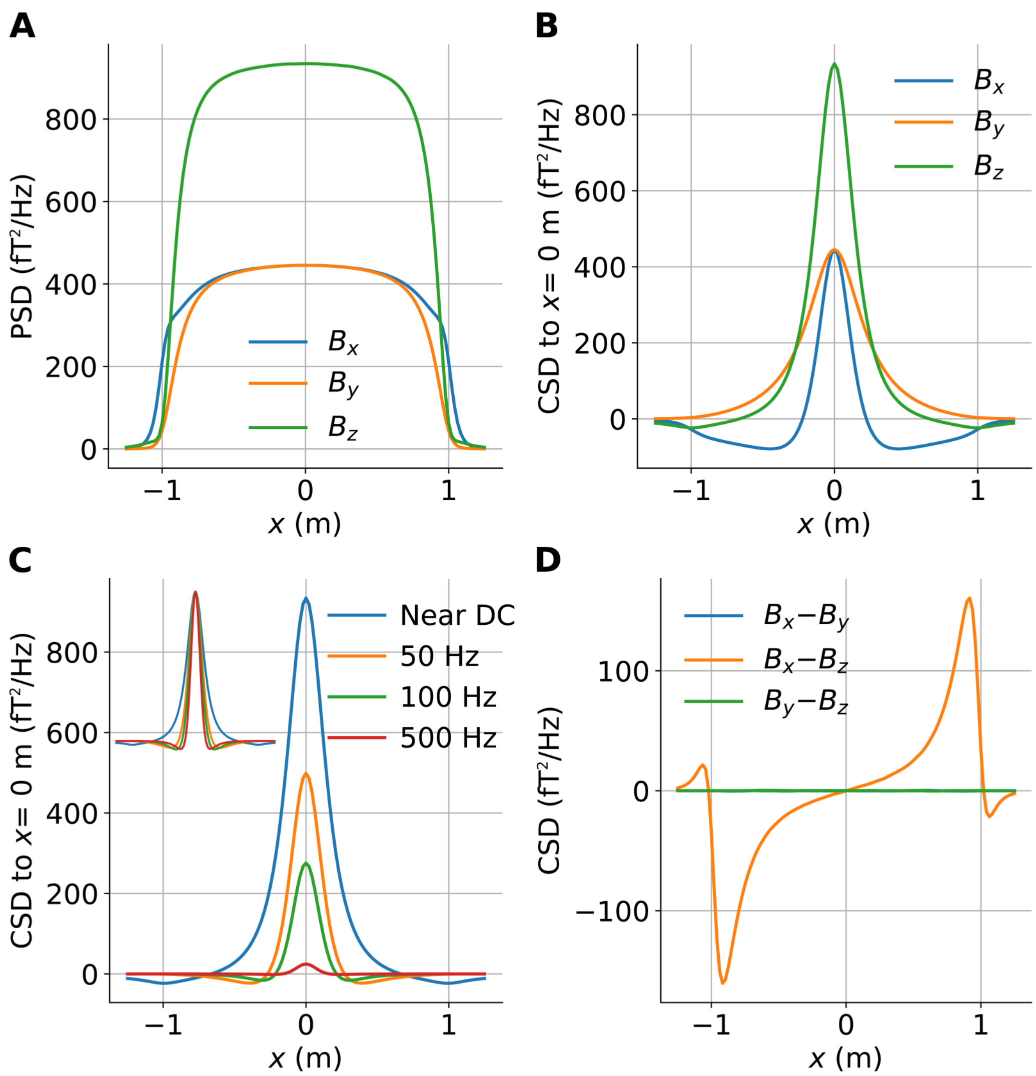

FIG. 4. Magnetic noise cross-spectral density (CSD) along the x axis ($z = 0.1R$) due to a conducting disk with radius $R = 1.0$ m centered on the xy plane. (a) Low-frequency noise power spectral density along the x axis. (b) Low-frequency noise CSD to $x = 0$ m. (c) Noise cross-spectral density of B_z to $x = 0$ m at different frequencies. The inset shows the amplitude-normalized cross-spectral density. (d) Noise CSD between different components of the magnetic field.

circular conducting disk centered on the xy plane [$R = 1$ m; mesh with 5418 triangles, Fig. 1(a)]. In these examples, we omit skin effects.

The spectral density of B_z noise due to the disk is shown in Fig. 3. The same figure also shows the estimated frequency at which the PSD is reduced by three decibels from the zero-frequency value. This -3-dB frequency $(4\mu_0\sigma\, dz)^{-1}$ for an infinite planar conductor[3] is also shown. At small relative distances to the disk ($z < 0.1R$), the numerical -3-dB frequencies scale as those for an infinite plane. At distances comparable to the radius $z \approx R$, the –3-dB frequency is constant, suggesting contribution of a single mode with the largest time constant.

Figure 4 shows examples of cross-spectral density of magnetic noise due to the disk calculated on the x axis. Close to the center of the disk, the PSDs of magnetic field components are nearly uniform with values of about 445.1, 445.3, and 932.2 $\mathrm{fT}^2/\mathrm{Hz}$ [for B_x^2, B_y^2, and B_z^2, respectively; Fig. 4(a)]. The ratio B_x^2/B_z^2 is approximately 0.48 near the center; for an infinite conductor, it has been shown to be $1/2$.[4] The cross-spectral density of B_z to the center of the disk ($x = 0$ m) decreases as a function of x as shown in Fig. 4(c). Moreover, at higher frequencies, the CSD falls off more rapidly with distance. For the disk, only B_x and B_z of the Cartesian magnetic field components are markedly correlated along the x axis [Fig. 4(d)], with the highest correlation being near the rim of the disk.

We then investigated magnetic noise due to a planar conductor with a star shape (1442 vertices, 2702 triangles). Figure 5 illustrates the noise-current patterns on the conductor and the magnetic noise spectral density at different perpendicular distances from the conductor. At small relative distances, the magnetic noise spectral density has a spatial structure that resembles the shape of the conductor. At larger distances, the magnetic noise loses structural detail, reflecting the different falloff distances of the field noise components that correspond to the noise-current modes with different levels of spatial detail. Close to the center of the conductor, the low-frequency values for B_x, B_y, and B_z noise are 18.15, 18.15, and 28.93 $\mathrm{fT}/\sqrt{\mathrm{Hz}}$, respectively. At higher frequency, the B_z amplitude is smaller but the star shape is a bit more pronounced.

Last, as a practical example, we computed the low-frequency magnetic-noise CSD seen by a helmet-shaped array of 102 magnetometers measuring the field component normal to the helmet surface as in a commercial magnetoencephalography (MEG) system (MEGIN Oy, Helsinki, Finland). We modeled the individual magnetometers using 16 field integration points as in the MNE-Python software.[27] We investigated two geometries depicted in Fig. 6. In the first geometry, the magnetometer array was near an aluminum plate; similar modeling for a finite-size sensor has also been done by Nenonen *et al.*[4] In the second geometry, the magnetometer array was inside a closed cylindrical aluminum shield. This geometry may be relevant for optically pumped magnetometer arrays in MEG, which can operate inside "person-sized" magnetically shielded cylinders.[28,29] However, we note that our method cannot currently model the magnetic noise from a system which consists of layers of both high-permeability and conductive materials. In both cases, the surface was room-temperature aluminum with a 5-mm thickness.

The estimated low-frequency noise CSD in the array is presented in Fig. 6. In the case of the aluminum plate, the magnetometers closest to the plate pickup the most noise. Magnetometer

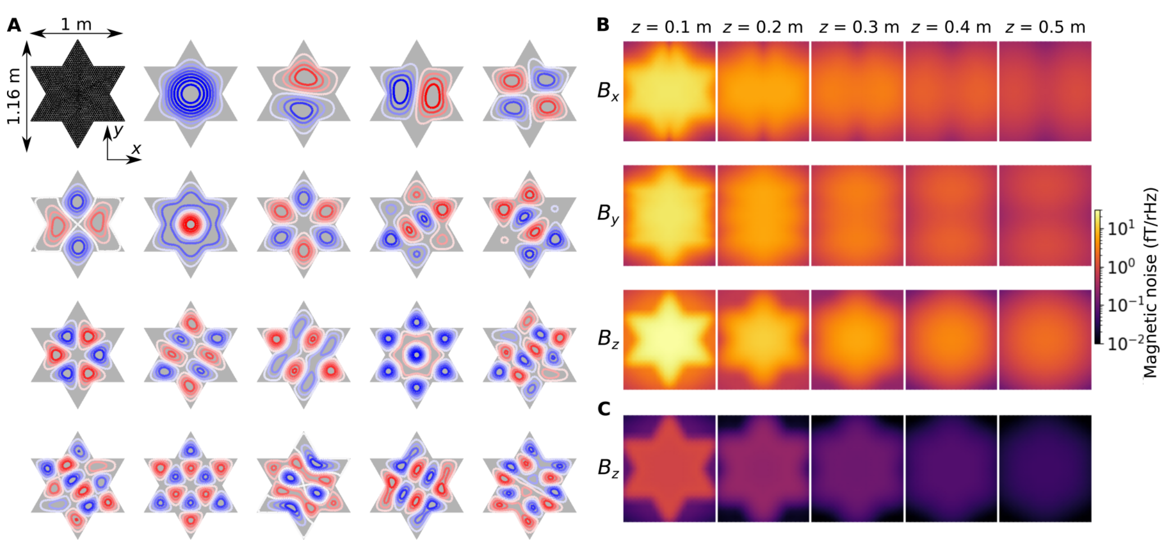

FIG. 5. Magnetic thermal noise due to a star-shaped planar conductor. (a) The triangle mesh representing the conductor and the numerically computed thermal current patterns on the conductor. The time constant of the patterns decreases from left to right and from top to bottom. Blue and red contours depict current flow in opposite directions. (b) Low-frequency noise spectral density at different vertical distances to the conductor. The plot limits are the same as the size of the conductor shown left. (c) B_z magnetic noise spectral density at 3 kHz.

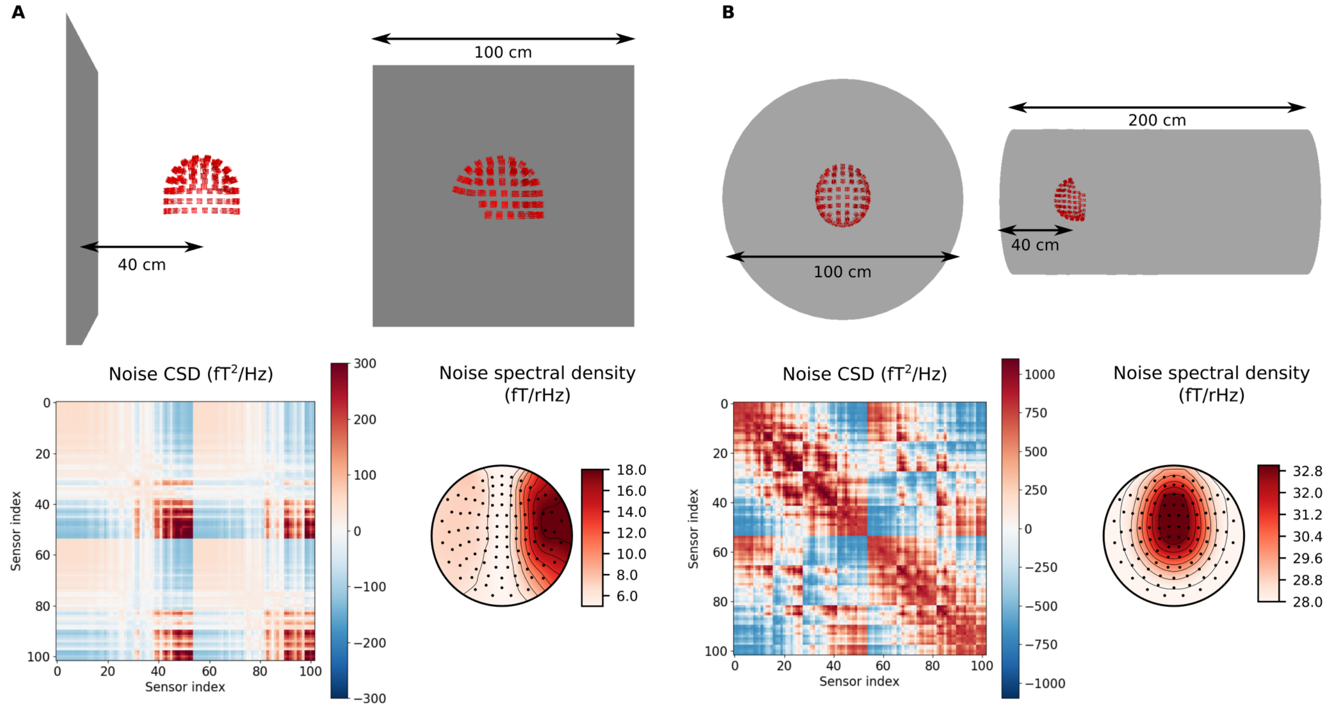

FIG. 6. Thermal magnetic-noise CSD at low frequencies as seen by a helmet-shaped array of 102 magnetometers. (a) The helmet near an aluminum plate. (b) The helmet inside a closed cylindrical aluminum shield. The noise spectral density is plotted as a topographic 2D projection of the sensor-array geometry (generated using the MNE-Python software[27]). The aluminum is at room temperature and has a thickness of 5 mm in both cases.

orientation also affects the noise level: the magnetometers on the sides of the helmet pickup more noise than those in the middle as the magnetic field component normal to the plate has the highest noise power. In the case of the cylindrical shield, the magnetometers near the vertex of the helmet pickup the most noise due to their proximity to the lid of the cylinder.

V. DISCUSSION

Overall, Fig. 1 gives a qualitative description of how the accuracy of the presented method depends on the mesh resolution and distance to the mesh. Generally, as the distance to the mesh decreases, a denser mesh is needed to get an accurate estimate of the magnetic noise. On the other hand, a denser mesh allows us to model higher order noise modes more accurately. As the order of the noise mode increases, the mode splits into smaller and smaller current loops with alternating directions of current flow. With the increasing mode order, the magnetic field generated by the mode decays more rapidly as a function of distance. Closer to the surface, the relative contributions of the higher order modes are larger, and a denser mesh is needed to better model both the modes and the magnetic noise.

The presented method can be extended to a wider range of systems; for instance, one could study a system of multiple separate but coupled conductors. Related to this, an interesting further direction is to model a single conductor as a set of thin inductively coupled conducting layers.[24] This could include models that account for the so-called skin effect that occurs at higher frequencies. In our preliminary computations regarding such a multilayer model of a disk, we obtained evidence of a frequency scaling of $f^{-3/4}$ for the magnetic noise in the skin-effect regime.[5] However, more work is needed to determine the accuracy of this approach in modeling the skin effect. This includes studying the inter-layer coupling model at different frequencies and geometries, taking into account the errors in the numerical integrals when using an increasingly dense packing of layers. Last, as another interesting development, we note that the model does not require the conductivity of the object to be constant, paving the way for calculation of noise from objects with non-uniform conductivity.

VI. CONCLUSION

We presented a method to compute the cross-spectral density of magnetic thermal noise due to a set of arbitrarily shaped conductors that can be considered surfaces, i.e., thin compared to the distances to the noise evaluation points. The numerical approach allows visualization of the noise-current patterns, providing an intuitive view on the underlying physics. We validated the numerical implementation by comparing the results to analytical formulas and found agreement within ~1%. The accuracy increased with the number of triangles in the discretized surface. We have made the implementation openly available as a part of the open-source Python software package bfieldtools.

ACKNOWLEDGMENTS

This work has received funding from the European Union's Horizon 2020 research and innovation programme under Grant Agreements No. 820393 (macQsimal) and No. 852111 (MAX-BAS) as well as from the European Research Council under ERC Grant Agreement No. 678578 (HRMEG). The content is solely the responsibility of the authors and does not necessarily represent the official views of the funding organizations.

The authors declare no conflicts of interest.

APPENDIX: MATRIX EQUATION

Here, we briefly present the derivation of the matrix equation (6) using the stream-function representation of the surface-current density [see Eq. (2)]. We start from Ohm's law and divide the electric field $\vec{E}$ into two components as

$$\begin{aligned}\vec{K}(\vec{r},t) &= \sigma(\vec{r})\,d(\vec{r})\vec{E}(\vec{r},t) = \sigma(\vec{r})\,d(\vec{r})\big(\vec{E}_s(\vec{r},t)+\vec{E}_p(\vec{r},t)\big)\\ &= \sigma(\vec{r})\,d(\vec{r})\left(-\frac{\partial\vec{A}(\vec{r},t)}{\partial t}-\nabla V+\vec{E}_p(\vec{r},t)\right),\end{aligned} \tag{A1}$$

where $\vec{E}_p$ is the primary field due to thermal motion of charge carriers and $\vec{E}_s$ is the macroscopic secondary field given as a sum of divergence- and curl-free components with corresponding vector and scalar potentials, $-\partial\vec{A}/\partial t$ and $-\nabla V$, respectively. The divergence-free component is due to the time-evolving current density $\vec{K}$ while the curl-free component is caused by charge redistribution enforcing the field tangential to the surface.

By reordering the terms and expressing the vector potential using the current density, Eq. (A1) reads

$$\frac{\partial}{\partial t}\frac{\mu_0}{4\pi}\int_S\frac{\vec{K}(\vec{r}\,',t)}{|\vec{r}-\vec{r}\,'|}\,dS'+\nabla V+\frac{\vec{K}(\vec{r},t)}{\sigma(\vec{r})\,d(\vec{r})}-\vec{E}_p(\vec{r},t)=0. \tag{A2}$$

We consider a frequency range where the macroscopic charge density does not fluctuate ($\nabla\cdot\vec{K}=0$); the current density can be expressed with the stream function,

$$\frac{\partial}{\partial t}\sum_k s_k(t)\frac{\mu_0}{4\pi}\int_S\frac{\vec{k}_k(\vec{r}\,')}{|\vec{r}-\vec{r}\,'|}\,dS'+\nabla V+\sum_k s_k(t)\frac{\vec{k}_k(\vec{r})}{\sigma(\vec{r})\,d(\vec{r})}-\vec{E}_p(\vec{r})=0. \tag{A3}$$

By taking a dot product with $\vec{k}_l(\vec{r})$ and integrating over the surface, we have

$$\begin{aligned}&\frac{\partial}{\partial t}\sum_k s_k(t)\frac{\mu_0}{4\pi}\int_S\int_S\frac{\vec{k}_l(\vec{r})\cdot\vec{k}_k(\vec{r}\,')}{|\vec{r}-\vec{r}\,'|}\,dS\,dS'+\int_S\vec{k}_l(\vec{r})\cdot\nabla V\,dS\\ &\quad+\sum_k s_k(t)\int_S\frac{\vec{k}_l(\vec{r})\cdot\vec{k}_k(\vec{r})}{\sigma(\vec{r})\,d(\vec{r})}\,dS-\int_S\vec{k}_l(\vec{r})\cdot\vec{E}_p(\vec{r},t)\,dS=0.\end{aligned} \tag{A4}$$

Denoting the tangential nabla operator as $\nabla_\parallel$, we can write $\vec{k}_l(\vec{r})\cdot\nabla V=(\nabla_\parallel\psi_l\times\hat{n})\cdot\nabla_\parallel V=-(\nabla_\parallel V\times\hat{n})\cdot\nabla_\parallel\psi_l=-\nabla_\parallel\cdot[(\nabla_\parallel V\times\hat{n})\psi_l]$. By applying the divergence theorem, the surface integral of the expression can be turned into a line integral over a closed path on the surface boundary, which is zero as ψ_l is constant on the boundary.[22]

The resistance and inductance matrix elements can be identified from Eq. (A4) to arrive at the equation system,

$$\sum_k M_{lk}\frac{\partial}{\partial t}s_k(t)+\sum_k R_{lk}s_k(t)-e_l(t)=0, \tag{A5}$$

where $e_l(t)=\int_S\vec{k}_l(\vec{r})\cdot\vec{E}_p(\vec{r},t)\,dS$ is the source emf coupled to the lth pattern.

DATA AVAILABILITY

The scripts and geometry files that were used to produce the presented results are available in the bfieldtools GitHub repository at https://github.com/bfieldtools/ (Ref 30).

REFERENCES

[1]J. B. Johnson, "Thermal agitation of electricity in conductors," Phys. Rev. **32**, 97–109 (1928).
[2]H. Nyquist, "Thermal agitation of electric charge in conductors," Phys. Rev. **32**, 110–113 (1928).
[3]T. Varpula and T. Poutanen, "Magnetic field fluctuations arising from thermal motion of electric charge in conductors," J. Appl. Phys. **55**, 4015–4021 (1984).
[4]J. Nenonen, J. Montonen, and T. Katila, "Thermal noise in biomagnetic measurements," Rev. Sci. Instrum. **67**, 2397–2405 (1996).
[5]S.-K. Lee and M. V. Romalis, "Calculation of magnetic field noise from high-permeability magnetic shields and conducting objects with simple geometry," J. Appl. Phys. **103**, 084904 (2008).
[6]S. Lamoreaux, "Feeble magnetic fields generated by thermal charge fluctuations in extended metallic conductors: Implications for electric-dipole moment experiments," Phys. Rev. A **60**, 1717–1720 (1999).
[7]C. T. Munger, Jr., "Magnetic Johnson noise constraints on electron electric dipole moment experiments," Phys. Rev. A **72**, 012506 (2005).
[8]C. Henkel, "Magnetostatic field noise near metallic surfaces," Eur. Phys. J. D **35**, 59–67 (2005).
[9]S. Uhlemann, H. Müller, J. Zach, and M. Haider, "Thermal magnetic field noise: Electron optics and decoherence," Ultramicroscopy **151**, 199–210 (2015).
[10]B. J. Roth, "Thermal fluctuations of the magnetic field over a thin conducting plate," J. Appl. Phys. **83**, 635–638 (1998).
[11]J. Clem, "Johnson noise from normal metal near a superconducting SQUID gradiometer circuit," IEEE Trans. Magn. **23**, 1093–1096 (1987).
[12]J.-H. Storm, P. Hömmen, D. Drung, and R. Körber, "An ultra-sensitive and wideband magnetometer based on a superconducting quantum interference device," Appl. Phys. Lett. **110**, 072603 (2017).
[13]J.-H. Storm, P. Hömmen, N. Höfner, and R. Körber, "Detection of body noise with an ultra-sensitive SQUID system," Meas. Sci. Technol. **30**, 125103 (2019).
[14]H. J. Sandin, P. L. Volegov, M. A. Espy, A. N. Matlashov, I. M. Savukov, and L. J. Schultz, "Noise modeling from conductive shields using Kirchhoff equations," IEEE Trans. Appl. Supercond. **21**, 489–492 (2010).
[15]I. Savukov and Y. J. Kim, "Investigation of magnetic noise from conductive shields in the 10–300 kHz frequency range," J. Appl. Phys. **128**, 234501 (2020).
[16]J. T. Harding and J. E. Zimmerman, "Quantum interference magnetometry and thermal noise from a conducting environment," Phys. Lett. A **27**, 670–671 (1968).

[17]A. Tervo, "Noise optimization of multi-layer insulation in liquid-helium cryostat for brain imaging," Master's thesis (Aalto University, 2016).
[18]D. T. Gillespie, "The mathematics of Brownian motion and Johnson noise," Am. J. Phys. **64**, 225–240 (1996).
[19]A. J. Mäkinen, R. Zetter, J. Iivanainen, K. C. J. Zevenhoven, L. Parkkonen, and R. J. Ilmoniemi, "Magnetic-field modeling with surface currents. Part I. Physical and computational principles of bfieldtools," J. Appl. Phys. **128**, 063906 (2020).
[20]R. Zetter, A. J. Mäkinen, J. Iivanainen, K. C. J. Zevenhoven, R. J. Ilmoniemi, and L. Parkkonen, "Magnetic field modeling with surface currents. Part II. Implementation and usage of bfieldtools," J. Appl. Phys. **128**, 063905 (2020).
[21]G. N. Peeren, "Stream function approach for determining optimal surface currents," J. Comput. Phys. **191**, 305–321 (2003).
[22]K. C. Zevenhoven, S. Busch, M. Hatridge, F. Öisjöen, R. J. Ilmoniemi, and J. Clarke, "Conductive shield for ultra-low-field magnetic resonance imaging: Theory and measurements of eddy currents," J. Appl. Phys. **115**, 103902 (2014).
[23]G. H. Golub and C. F. Van Loan, *Matrix Computations* (JHU Press, 2012), Vol. 3.
[24]H. Sanchez Lopez, F. Freschi, A. Trakic, E. Smith, J. Herbert, M. Fuentes, S. Wilson, L. Liu, M. Repetto, and S. Crozier, "Multilayer integral method for simulation of eddy currents in thin volumes of arbitrary geometry produced by MRI gradient coils," Magn. Reson. Med. **71**, 1912–1922 (2014).
[25]P. Virtanen, R. Gommers, T. E. Oliphant, M. Haberland, T. Reddy, D. Cournapeau, E. Burovski, P. Peterson, W. Weckesser, J. Bright *et al.*, SciPy 1.0: Fundamental algorithms for scientific computing in Python," Nat. Methods **17**, 261–272 (2020).
[26]T. E. Oliphant, *A Guide to NumPy* (CreateSpace Independent Publishing Platform, 2015), Vol. 1.
[27]A. Gramfort, M. Luessi, E. Larson, D. A. Engemann, D. Strohmeier, C. Brodbeck, L. Parkkonen, and M. S. Hämäläinen, "MNE software for processing MEG and EEG data," Neuroimage **86**, 446–460 (2014).
[28]A. Borna, T. R. Carter, J. D. Goldberg, A. P. Colombo, Y.-Y. Jau, C. Berry, J. McKay, J. Stephen, M. Weisend, and P. D. Schwindt, "A 20-channel magnetoencephalography system based on optically pumped magnetometers," Phys. Med. Biol. **62**, 8909 (2017).
[29]K. He, S. Wan, J. Sheng, D. Liu, C. Wang, D. Li, L. Qin, S. Luo, J. Qin, and J.-H. Gao, "A high-performance compact magnetic shield for optically pumped magnetometer-based magnetoencephalography," Rev. Sci. Instrum. **90**, 064102 (2019).
[30]J. Iivanainen (2021). "Added scripts to reproduce the computations of the thermal magnetic noise manuscript," bfieldtools GitHub repository https://github.com/bfieldtools/bfieldtools/commit/ba28360930b1905155be70abad558588e0fe14eb.